

CONTROLLED TOPOLOGICAL TRANSITIONS IN THIN-FILM PHASE SEPARATION*

MATTHEW G. HENNESSY[†], VICTOR M. BURLAKOV[†], ALAIN GORIELY[†], BARBARA
WAGNER[‡], AND ANDREAS MÜNCH[†]

Abstract. In this paper the evolution of a binary mixture in a thin-film geometry with a wall at the top and bottom is considered. By bringing the mixture into its miscibility gap so that no spinodal decomposition occurs in the bulk, a slight energetic bias of the walls toward each one of the constituents ensures the nucleation of thin boundary layers that grow until the constituents have moved into one of the two layers. These layers are separated by an interfacial region where the composition changes rapidly. Conditions that ensure the separation into two layers with a thin interfacial region are investigated based on a phase-field model. Using matched asymptotic expansions a corresponding sharp-interface problem for the location of the interface is established. It is then argued that this newly created two-layer system is not at its energetic minimum but destabilizes into a controlled self-replicating pattern of trapezoidal vertical stripes by minimizing the interfacial energy between the phases while conserving their area. A quantitative analysis of this mechanism is carried out via a thin-film model for the free interfaces, which is derived asymptotically from the sharp-interface model.

Key words. phase separation in confined geometry, sharp-interface asymptotics, thin-film equations, topological transformations

AMS subject classifications. 35B40, 76M45, 76E17

DOI. 10.1137/130950227

1. Introduction. Structure formation in mixtures such as polymer blends and metal or semiconductor alloys is abundant in nature and in many technological processes. This phenomenon generally occurs when, due to a change in the external conditions such as temperature, pressure, applied stresses, or a change in the composition, it becomes energetically preferable for the materials to be in a nonhomogeneous structured state rather than the homogeneous state. The system will tend to a new minimum of its associated total free energy by undergoing phase transformations through spinodal decomposition or nucleation events, thereby forming new spatial domains with different composition, polymer phases, crystal structure or orientation, giving rise to new material properties. The new interfaces that bound these domains coarsen on much slower time scales until a global energetic minimum has been reached. For a review on structure forming processes in materials see, for example, Binder and Fraztl [2].

*Received by the editors December 23, 2013; accepted for publication (in revised form) October 9, 2014; published electronically January 6, 2015.

<http://www.siam.org/journals/siap/75-1/95022.html>

[†]Mathematical Institute, University of Oxford, Andrew Wiles Building, Radcliffe Observatory Quarter, Woodstock Road, Oxford, OX2 6GG, UK (hennessy@maths.ox.ac.uk, victor.burlakov@maths.ox.ac.uk, alain.goriely@maths.ox.ac.uk, muench@maths.ox.ac.uk). The work of these authors was supported by KAUST (award KUK-C1-013-04). The second and third authors were also supported by the James Martin School. The third author is a Wolfson/Royal Society Merit Award Holder and acknowledges support from a reintegration grant under EC Framework VII.

[‡]Technische Universität Berlin, Institute of Mathematics, Straße des 17. Juni 136, 10623 Berlin, Germany, and Weierstrass Institute, Mohrenstraße 39, 10117 Berlin, Germany (bwagner@math.tu-berlin.de). This author's work was supported by the Federal Ministry of Education (BMBF) and the state government of Berlin (SENBF) in the framework of the program "Spitzenforschung und Innovation in den Neuen Ländern" (grant 03IS2151).

Throughout the whole process different physical effects and material properties such as interfacial stresses, elastic strains, chemical reactions at interfaces, electrostatic forces, and bulk and interfacial diffusion may have to be taken into account. Moreover, in confined geometries, as is the case for most nano-technological applications, the influence of nearby walls will have a significant impact on the phase separation either by introducing additional geometric length scales or through their surface energies which determine their wetting properties.

For a thermally quenched mixture in a confined geometry it has been shown, experimentally [17, 20] and theoretically [3], that phase separation can be induced by the interface energy of the nearby walls. Various scenarios of these so-called surface-directed phase separation phenomena have been investigated on the basis of appropriate boundary value problems for the stochastic Cahn–Hilliard model, including off-critical quenches, i.e., where no phase separation would occur for unconfined case; see Puri and Binder [27]. Their numerical results exhibit cases where typical bulk phase separation occurs together with a wetting layer as well as cases where only the growing wetting layer emerges. These studies were extended further using different free energies and different intermolecular potentials; see Brown and Chakrabarti [4] or Yan et al. [33] for a discussion of these models.

Similarly, during spin-coating of a mixture of two polymers blended in a common volatile solvent, a stratified film of nano- to micrometer thickness that exhibits an internal interfacial microstructure is produced. Several experimental studies using PFB/F8BT and PS/PMMA systems have suggested that phase separation starts in such processes with the formation of a vertically stratified bilayer, followed by a destabilization of the polymer-polymer interface that is thought to be caused by a solvent-concentration gradient through the film [13, 14, 18, 30].

Developing a systematic quantitative understanding of such complex evolutionary processes is the key to predicting and controlling the structure morphology and hence the material properties, such as the optical and electrical properties of the active component of organic polymer-polymer solar cells, or other advanced multifunctional materials. In Hennessy et al. [12], a new mechanism that induces a well-defined sequence of repeating structures in a geometrically confined binary mixture is presented. A qualitative argument is given to explain how a horizontal bilayer state may transition into a striped state of alternating phases. The metastable horizontal layered state enters a cascade of rupture events that leads to a state with regular well-defined trapezoidal stripes, minimizing their interfacial energies.

The focus of the present study is to develop the theory behind the transition mechanism described in Hennessy et al. [12] and to determine under which conditions the horizontal bilayer state can form while allowing for subsequent stripe formation. Classical ways to create a bilayer include imposing an external field that is switched off, placing the two layers on top of each other, and using initial compositional gradients that can selectively drive the coarsening of the structured state created by the initial phase separation and give rise to long-lived metastable bilayer states [15]. However, here we will explore another possibility. In particular, we use surfaces that are biased toward one of the components and then bring the system slowly into the miscibility gap. The bias of the walls will create a slight compositional gradient across the thin film between the substrates that continues to build up as the species are driven toward separation.

Within the framework of a phase-field theory of Cahn–Hilliard type with appropriate surface energies at the walls, which we introduce in section 2, we address the question of when the mixture phase separates into two horizontal layers with a dif-

fuse interface that is thin compared to the transversal length scale of the thin film in section 3. The scale separation between the large homogeneous regions and the thin regions of steep compositional changes are then exploited in section 4 to reduce the model to a sharp-interface model via the method of matched asymptotic expansions. Here we point out that for cases where the interfaces do not intersect an exterior boundary, such as a wall, the derivation of such models go back to Pego [25] and were subsequently analyzed by Alikakos, Bates, and Chen [1] and Chen [8]. For the cases where the interfaces intersect an exterior boundary, which is the focus of our investigation, an additional condition at the contact line is required. We use the expression derived rigorously through a sharp-interface limit for the stationary Cahn–Hilliard equation by Modica [21]. The expression yields a Young-type condition for the contact angle in terms of the surface free energy contribution from the walls that closes the sharp-interface model.

We further exploit the separation between the lateral and the vertical length scales of the sharp-interface profile to derive a thin-film model for the free interface. This model greatly facilitates the systematic quantitative numerical study. It also enhances our understanding of the dynamics via the mathematical properties of the associated thin-film boundary value problem. This is used to discuss the bilayer breakup in section 5. In section 6, we give our conclusions and an outlook.

2. Formulation of the phase-field model.

Bulk equations. For a mixture of two species, A and B , that undergo phase separation below a critical temperature, $T = T_c$, we introduce a phase-field model based on the Cahn–Hilliard equation. Besides the original work by Cahn and Hilliard [7] and by Cahn [5], there is a vast original literature and reviews on such types of phase-field models including differences in the derivation and the scope of the modeling [24, 23, 26, 11]. In our formulation, the phase-field parameter ϕ is a conserved order parameter, obtained, for example, as a scaled volume or mole fraction, where $\phi = 1$ represents the pure A species and $\phi = -1$ the pure B species, and $\phi = 0$ a symmetric, or 50:50 mixture of the two species. The nondimensional bulk equations in the domain $\Omega = \{(x, z) : x \in \mathbb{R}, 0 < z < d\}$ are given by

$$(2.1a) \quad \phi_t = \nabla \cdot [(1 - \phi^2)\nabla\mu],$$

$$(2.1b) \quad \mu = \frac{1}{T} [f'(\phi) - \varepsilon^2 \Delta\phi],$$

$$(2.1c) \quad f(\phi) = -\phi^2 + T[(1 - \phi)\ln(1 - \phi) + (1 + \phi)\ln(1 + \phi)],$$

where μ is the chemical potential and T is the temperature. We will vary the temperature and therefore the explicit dependence on T has been retained in (2.1b). The parameter ε is the ratio of the microscopic length scale of the interaction between the two species—a quantity that can be expressed in terms of the lattice parameter in the case of nearest neighbor interactions in a cubic lattice; see, for example, Cahn and Hilliard [7]—and the macroscopic length scale used to nondimensionalize the system. For the latter, we can assume, for example, the thickness of one of the layers in the bilayer state that we will investigate has been scaled to one.

The boundary conditions are

$$(2.2a) \quad \mu_z = 0, \quad \varepsilon\phi_z = f'_0(\phi) \quad \text{at } z = 0,$$

$$(2.2b) \quad \mu_z = 0, \quad \varepsilon\phi_z = f'_0(-\phi) \quad \text{at } z = d,$$

where the left two conditions, $\mu_z = 0$, correspond to no flux through the substrate, and the other two represent the interaction of the species with the substrate. The

specific choice of the substrate-material interaction energy, f_0 , is introduced further below. The results of Modica [21] enable effective surface energies of material-wall interfaces to be derived from the interaction potential f_0 . These can be used in a Young-like expression to determine the equilibrium contact angle that forms when an A - B interface comes in contact with a wall. Mathematical details of this are given in section 4.

The chemical potential and the latter two boundary conditions arise as the first variation of the free energy F/T of the system, where the functional F is given by

$$(2.3) \quad \begin{aligned} F[\phi] = & \int_0^d \int_{-\infty}^{+\infty} f(\phi(x, z)) + \frac{\varepsilon^2}{2} |\nabla \phi(x, z)|^2 \, dx dz \\ & + \varepsilon \int_{-\infty}^{+\infty} f_0(\phi(x, 0)) \, dx + \varepsilon \int_{+\infty}^{-\infty} f_0(-\phi(x, d)) \, dx. \end{aligned}$$

For T below the critical temperature T_c , which here has been scaled to one, the homogeneous contribution f to the bulk has a double-well structure and will drive the system to phase separate into domains with compositions that correspond to the minima of f . The choice of substrate-material interface energy density assumes antisymmetric substrates since the integrand in the substrate integral at $z = 0$ is transformed into the integrand of the integral at $z = d$ if ϕ is replaced by $-\phi$. Thus, the affinity of the upper substrate to species A is the same as the affinity of the lower substrate to B . Using such interface energy distributions assumes that we only consider short-range surface interactions; other possibilities include contributions to the bulk free energy [28].

We are mostly interested in phase-separating situations close to criticality, with T below and close to 1, where the minima of f , denoted by ϕ_{\pm} , are close to zero. In addition, we intend to consider different choices for the temperature and, in section 3, we also prescribe time-dependent temperature profiles. Thus, we let $(1/T - 1) = \chi_0 \chi(t)$ with a new parameter $\chi_0 \ll 1$, and a function $\chi(t)$, where $0 \leq \chi(t) \leq 1$. It is then convenient to let

$$(2.4) \quad \phi = (3\chi_0)^{1/2} \hat{\phi}, \quad \mu = 3^{1/2} \chi_0^{3/2} \hat{\mu}, \quad t = \varepsilon^{-1} (\chi_0 + \chi_0^2)^{-1/2} \hat{t},$$

in (2.1), (2.2), so that, to leading order in $\chi_0 \ll 1$, we obtain

$$(2.5a) \quad \hat{\varepsilon} \hat{\phi}_{\hat{t}} = \Delta \hat{\mu},$$

$$(2.5b) \quad \hat{\mu} = \hat{f}'(\hat{\phi}) - \hat{\varepsilon}^2 \Delta \hat{\phi},$$

$$(2.5c) \quad \hat{f}(\hat{\phi}) = \frac{1}{2} (\hat{\phi}^2 - \chi(t))^2,$$

where $\hat{\varepsilon} \equiv \varepsilon(1 + 1/\chi_0)^{1/2}$. We remark that in section 4.1 we will consider a sharp-interface limit where $\hat{\varepsilon} \ll 1$ which effectively puts a lower bound on the value of χ_0 , namely, $\varepsilon^2 \ll \chi_0$. Furthermore, \hat{f} has been altered by a ϕ -independent function of time, which is immaterial here. By a suitable rescaling of the substrate-material interaction energy, f_0 , the corresponding boundary conditions for the order parameter may be written as

$$(2.5d) \quad \hat{\varepsilon} \hat{\phi}_z = \hat{f}'_0(\hat{\phi}), \quad z = 0,$$

$$(2.5e) \quad \hat{\varepsilon} \hat{\phi}_z = \hat{f}'_0(-\hat{\phi}), \quad z = d,$$

where the prime now denotes differentiation with respect to $\hat{\phi}$. Commonly used expressions for \hat{f}_0 involve quadratic or cubic polynomials which can be thought of as truncated power series expansions about a given state [27]. In this paper, we take \hat{f}_0 to be cubic and of the form

$$(2.5f) \quad \hat{f}_0(\hat{\phi}) = \hat{\beta}(\hat{\phi} - \hat{\phi}^3/3),$$

where $\hat{\beta}$ provides a measure of how biased each wall is to its preferred species. The advantage of using (2.5f) is that its minima coincide with those of the homogeneous free energy f when $\chi = 1$, which makes it convenient [32] to relate the parameter $\hat{\beta}$ to the equilibrium contact angle θ using the results of Modica [21]. Further details of this are given in section 4. Using (2.5f) in (2.5d), the full set of rescaled boundary conditions are given by

$$(2.5g) \quad \hat{\mu}_z = 0, \quad \hat{\varepsilon}\hat{\phi}_z = \hat{\beta}(1 - \hat{\phi}^2) \quad \text{at } z = 0, d.$$

In the following, we drop the hats from all variables and parameters.

3. Formation of bilayers. Using the model developed in the previous section, we can now investigate the conditions in which the two constituent components of the mixture separate and form a horizontal bilayer. This investigation will be guided by linear stability results and numerical simulations. We assume that the initial condition is a small random perturbation with mean value zero to the homogeneous 50:50 state (the latter of which corresponds to $\phi \equiv 0$). We typically set $\varepsilon = 0.127$ and for the numerical simulations, the domain is truncated at $x = 0$ and $x = L_\infty$, with $L_\infty \gg d$, and we impose periodic boundary conditions.

For definiteness and to facilitate the discussion we interpret the function $\chi(t)$ as the temperature of the system in the remaining part of our study. The arguments, however, are general and can equally be made for other realizations, such as the concentration of the species.

Stability analysis. We investigate the linear stability of one-dimensional stationary solutions when the temperature is held at a constant value. Thus, we set $\chi(t) \equiv \chi$ and write the order parameter and the chemical potential as

$$(3.1a) \quad \phi(x, z, t) = \bar{\phi}(z) + \alpha\tilde{\phi}(z)e^{\lambda t + ikx},$$

$$(3.1b) \quad \mu(x, z, t) = \bar{\mu}(z) + \alpha\tilde{\mu}(z)e^{\lambda t + ikx},$$

where bars are used to represent the stationary solution and tildes denote perturbations to it. The parameters $\alpha \ll 1$, λ , and k denote the initial amplitude of the perturbation and its growth rate and wavenumber, respectively. The solution (3.1) is inserted into the governing equations and their boundary conditions (2.5), and the system is expanded in powers of α . We treat α as infinitesimal so that the inequality $\alpha \ll \varepsilon^2 \ll 1$ is always satisfied. We note that terms of $O(\varepsilon)$ play an important role in regularizing the problem; see Novick-Cohen [24] for more details.

The $O(1)$ contribution to this system describes the steady, one-dimensional problem. From this we find that the chemical potential satisfies $\bar{\mu}_{zz} = 0$ with $\bar{\mu}_z = 0$ on the boundaries. Therefore, the chemical potential is constant to leading order and we write $\bar{\mu}(z) \equiv \bar{\mu}$. The problem for the order parameter can be written as

$$(3.2a) \quad \bar{\mu} = f'(\bar{\phi}) - \varepsilon^2\bar{\phi}_{zz}$$

with boundary conditions

$$(3.2b) \quad \varepsilon \bar{\phi}_z = \beta (1 - \bar{\phi}^2), \quad z = 0, d.$$

The chemical potential is treated as a Lagrange multiplier that ensures the steady solution corresponds to a 50:50 mixture; thus, we supplement the boundary value problem with the integral condition given by

$$(3.2c) \quad \int_0^d \bar{\phi}(z) dz = 0.$$

The stability of the stationary solution is determined from the $O(\alpha)$ problem, which can be written as

$$(3.3a) \quad \varepsilon \lambda \tilde{\phi} = -k^2 \tilde{\mu} + \tilde{\mu}_{zz},$$

$$(3.3b) \quad \tilde{\mu} = f''(\bar{\phi}) \tilde{\phi} - \varepsilon^2 (-k^2 \tilde{\phi} + \tilde{\phi}_{zz})$$

with boundary conditions

$$(3.3c) \quad \tilde{\mu}_z = 0, \quad \varepsilon \tilde{\phi}_z = -2\beta \bar{\phi} \tilde{\phi}, \quad z = 0, d.$$

Given that the steady solution $\bar{\phi}$ is generally a function of space, the linear stability problem is nonautonomous and can be solved only in exceptional circumstances. Such is the case when the substrate-material interface energy is neglected, i.e., when $\beta = 0$, or when it is very small, $\beta \ll 1$. In both instances the steady solution is given by $\bar{\phi} \equiv 0$ (or to leading order in the latter case) and the perturbations take the form

$$(3.4) \quad \tilde{\phi}(z) = \tilde{\phi}_n \cos(n\pi z/d), \quad \tilde{\mu}(z) = \tilde{\mu}_n \cos(n\pi z/d),$$

where $n \in \mathbb{Z}$. The linearized problem can be solved and the growth rates are found to be

$$(3.5) \quad \lambda(\xi) = -\varepsilon^{-1} \xi^2 (\varepsilon^2 \xi^2 - 2\chi),$$

where $\xi^2 = k^2 + (n\pi/d)^2$ represents an average wavenumber that is composed of a continuous horizontal wavenumber k and a discrete vertical wavenumber n . Perturbations with average wavenumbers that satisfy

$$(3.6) \quad 0 < \xi^2 < \xi_c^2 = \frac{2\chi}{\varepsilon^2}$$

have positive growth rates and hence the one-dimensional stationary solution is linearly unstable. The fastest-growing perturbations have wavenumbers that satisfy $\xi_m = \xi_c/\sqrt{2}$ and these lead to the formation of distinct domains that are rich in one particular phase. The initial size of these domains is approximately equal to half of the wavelength of the fastest-growing modes.

The growth of perturbations with wavenumbers in the range given by (3.6) will eventually violate the conditions on which the linear stability problem was formulated, i.e., disturbances to the stationary state are small. When this happens, nonlinear effects begin to saturate perturbation growth. Physically, these effects correspond to a slow coarsening of nearly pure domains until the total interfacial area between them reaches a minimum. Due to the assumption of the film being longer than it is wide, it

becomes energetically favorable for the system to form domains that resemble a series of vertical columns instead of a horizontal bilayer.

When $\beta \neq 0$, the energetic interactions between the substrates and the constituent materials induce a layered morphology in the steady state solution of the one-dimensional problem. Examples of these solutions have been computed numerically and are shown as stars in Figures 1(d)–(f) when $\beta = 0.032$ and for temperatures given by $\chi = 0.01, 0.18, \text{ and } 1$, respectively. For temperatures below but close to criticality (panel (d)), the steady state solution resembles a small, approximately linear perturbation to the homogeneous 50:50 state. For cooler temperatures, the solutions correspond to bilayer configurations (panels (e) and (f)). By solving the corresponding linear stability problem numerically as well, we find that these steady states are linearly stable; that is, the growth rates are negative for each value of the perturbation wavenumber k . The functional forms of λ , i.e., $\lambda = \lambda(k)$, are shown in Figures 1(g)–(i).

In the case when $\varepsilon \ll 1$ and $\chi = 1$, the stability problem can be solved by matched asymptotic expansions. The leading-order composite solution to the stationary problem corresponds to a bilayer and is given by

$$(3.7a) \quad \bar{\phi}(z) = \tanh\left(\frac{z-1}{\varepsilon}\right).$$

The perturbation to the order parameter and its growth rate are, to leading order, given by

$$(3.7b) \quad \tilde{\phi}(z) = \operatorname{sech}^2\left(\frac{z-1}{\varepsilon}\right),$$

$$(3.7c) \quad \lambda(k) = -\frac{2}{3}k^3 \tanh(k),$$

respectively. Comparisons of the asymptotic and numerical stationary solution and growth rates are shown in Figures 1(f) and (i). The agreement between the stationary solutions is excellent, and the match between growth rates is also good, particularly when the wavenumber k is small.

The linear stability of the bilayer configuration over a wide range of temperatures suggests that a robust method for driving the system into such a state is to slowly cool the system from a near-critical temperature. By starting from a temperature close to the critical value, the influence of the substrates will induce a layered morphology and push the mixture toward its stable steady state profile. Decreasing the temperature at a sufficiently slow rate will then allow the mixture to evolve in a quasi-stationary manner that follows the steady state profile, thus yielding a bilayer configuration for cooler temperatures. The stability of the stationary layered profiles ensures that small fluctuations to the system will not be amplified during cooling and lead to alternative morphologies.

Numerical solution of the phase-field model. The numerical simulations are based on an implicit-explicit spectral method. The time derivative is discretized using the standard first-order finite difference approximation and any linear terms are handled implicitly, whereas nonlinear terms are treated explicitly. The solutions are assumed to be periodic in the horizontal direction and hence derivatives with respect to x are computed using Fourier spectral methods. Chebyshev spectral methods are used to compute derivatives in the vertical direction.

Using this numerical scheme, we first explore the dynamics that occur when the temperature of the system is fixed at a constant value that is below criticality. The

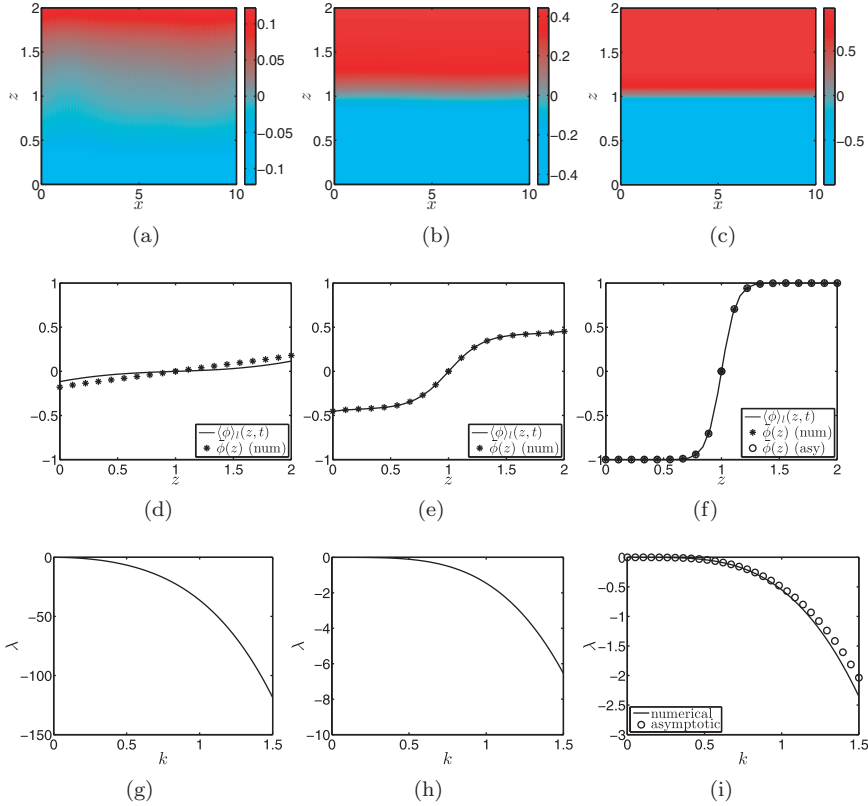


FIG. 1. Bilayer formation when the temperature of the system is slowly decreased according to the function $\chi(t) = 1 - \exp(-t/\tau_c)$ with $\tau_c = 51$. The initial condition was a randomly perturbed homogeneous 50:50 mixture. A-rich and B-rich domains are shown as red and blue, respectively. (a)–(c) Evolution of the order parameter. The solution is shown at times $t = 0.51, 10,$ and 253 , corresponding to $\chi(t) = 0.01, 0.18,$ and 1 , respectively. (d)–(f) Comparison of the laterally averaged order parameter $\langle\phi\rangle_l$ (solid line) with the instantaneous stable steady state solution (stars) at the same times as in panels (a)–(c). (g)–(i) The growth rate λ of perturbations to the steady state solutions shown above as functions of the perturbation wavenumber k . See text for the definition of $\langle\phi\rangle_l$ and the specific choice of τ_c that was used. The asymptotic solutions in panels (f) and (i) are given in (3.7).

interface energy between the substrates and the components is also taken into consideration. Thus, we set $\chi \equiv 1$ and $\beta = 0.032$. The computational domain is $L_\infty = 10$, and the initial condition is a random perturbation of amplitude 0.2 to the homogeneous 50:50 state. The simulation results, which are shown in Figure 2, indicate that the initial fluctuations in the solution are rapidly amplified by spinodal decomposition, producing small domains that are nearly pure in the two constituent species. The width of these domains in Figure 2(b) is approximately 0.4, which is in good agreement with the size that is predicted from the linear stability analysis; in this case the wavenumber of the fastest growing mode is $\xi_m \simeq 7.9$. For $t > 2.5 \times 10^{-4}$, these domains coarsen to form large-scale structures that eventually settle into columns.

We now investigate how the system evolves when it is slowly cooled from the critical temperature. In particular, the temperature is decreased according to $\chi(t) = 1 - \exp(-t/\tau_c)$ with $\tau_c = 51$. The values of the other parameters are the same as in Figure 2; we take $\beta = 0.031$, $L_\infty = 10$. The initial noise has an amplitude of 0.2 and is

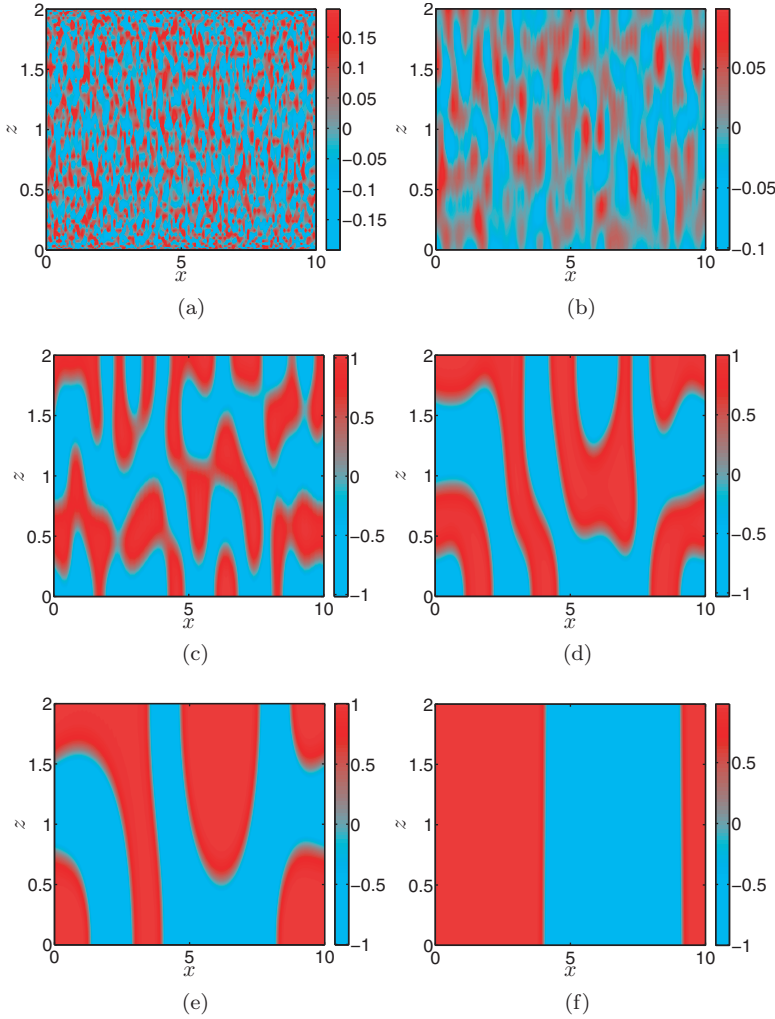


FIG. 2. Spinodal decomposition and coarsening in a system held at a constant temperature below the critical value. The temperature was fixed at $\chi \equiv 1$ and the initial condition was a randomly perturbed homogeneous 50:50 mixture. The solution is shown at times $t = 0, 2.5 \times 10^{-4}, 2.5 \times 10^{-2}, 0.10, 0.51,$ and 7.3 . Red and blue correspond to A -rich and B -rich domains, respectively.

similar to the initial condition shown in Figure 2(a). The results of the simulation are presented in Figure 1. Panels (a)–(c) of the figure display the evolution of the order parameter, whereas panels (d)–(f) compare, at various times, the laterally averaged order parameter, defined as

$$(3.8) \quad \langle \phi \rangle_l(z, t) = \frac{1}{L_\infty} \int_0^{L_\infty} \phi(x, z, t) dx,$$

to the instantaneous, stable steady state solution of the one-dimensional problem. The figure clearly shows that the cooling procedure is able to produce the bilayer morphology for parameter values that lead to a columnar topology when the temperature was held at a fixed value. The comparison of the laterally averaged order parameter and the stable steady state shows that the solution adopts the steady state profile and evolves in a quasi-stationary manner to the bilayer state.

The system will also tend to a bilayer configuration if the substrate-material interface energy is high. However, in this case it is possible for the bilayer state to minimize globally the energy of the system and hence it would be expected to be stable. That is, no topological transition could be initiated by nucleating a hole in the bilayer. This situation relates to the substrates being perfectly wetting, so that any hole in the bilayer will close up.

4. Asymptotic approximations.

4.1. Sharp-interface limit. For the topological transition, we will consider the system at a fixed temperature corresponding to $\chi = 1$. At this temperature, the width of the diffuse interface between A -rich and B -rich domains is $O(\varepsilon)$. Thus, for $\varepsilon \ll 1$, the thickness of the transition layer is small and the phase-field model (2.5) can be reduced to a sharp-interface model as described, for example, by Pego [25]. The order parameter and the chemical potential are written as an asymptotic series of the form

$$(4.1a) \quad \phi = \phi_0 + \varepsilon\phi_1 + O(\varepsilon^2),$$

$$(4.1b) \quad \mu = \varepsilon\mu_1 + O(\varepsilon^2).$$

The leading-order solution for the order parameter is $\phi_0 = \pm 1$. The $O(\varepsilon)$ problem is given by

$$(4.2a) \quad \Delta\mu_1 = 0$$

in the regions $0 < z < h(x, t)$ and $h(x, t) < z < d$. Along the sharp interface $z = h(x, t)$ we have the boundary conditions

$$(4.2b) \quad 2\mu_1 = \frac{\sigma h_{xx}}{(1 + h_x^2)^{3/2}},$$

$$(4.2c) \quad h_t = \frac{1}{2} ([\mu_{1,x}]_+^+ h_x - [\mu_{1,z}]_-^+).$$

The parameter σ is defined through the expression

$$(4.2d) \quad \sigma = \int_{-\infty}^{\infty} (\Phi_{0,\eta\eta})^2 d\eta = \frac{4}{3},$$

where Φ_0 is the solution to the leading-order inner problem given by $2(\Phi_0^3 - \Phi_0) = \Phi_{0,\eta\eta}$ subject to $\Phi_0 \rightarrow \pm 1$ as $\eta \rightarrow \pm\infty$ and $\Phi_0 = 0$ at $\eta = 0$. The solution is given by $\Phi_0 = \tanh \eta$, which can be directly used to show $\sigma = 4/3$.

Along the substrates $z = 0$ and $z = d$ we have the conditions

$$(4.2e) \quad \mu_{1,z} = 0.$$

The corresponding leading-order composite solution for a known sharp interface $h(x)$ is useful to know, in particular, when constructing initial conditions for the phase-field model. This solution can be written as

$$(4.3) \quad \phi(x, z) = \tanh \left(\frac{z - h(x)}{\varepsilon \sqrt{1 + h_x^2}} \right),$$

which is a generalization of the expression presented in (3.7a).

Where the interface touches a substrate, a condition for the contact angle is needed. In the limit considered here, the system is nearly in equilibrium, so we use the equilibrium contact angle which can be expressed in terms of the surface and interface energies via a Young–Laplace formula,

$$(4.4a) \quad \cos \theta = \frac{\gamma(1) - \gamma(-1)}{\bar{\sigma}},$$

with

$$(4.4b) \quad \bar{\sigma} = \int_{-1}^1 (2f(r))^{1/2} dr = \sigma = \frac{4}{3},$$

and where the appropriate surface energies need to include contributions from boundary layers near the substrates [6],

$$(4.4c) \quad \gamma(\rho) = \inf_{\omega} \left\{ f_0(\omega) + \left| \int_{\omega}^{\rho} (2f(r))^{1/2} dr \right| \right\}.$$

A rigorous proof of (4.4) is given by Modica [21]. If $\beta \leq 1$ one finds that $\gamma(\pm 1) = f_0(\pm 1) = \pm 2\beta/3$. The expression for the contact angle reduces to

$$(4.5) \quad \cos \theta = \beta.$$

Since we have assumed that the interface is given as the graph of a function $z = h(x, t)$, we need to restrict $0 \leq \theta \leq \pi/2$. The conditions at the contact line $x = s(t)$ are

$$(4.6) \quad h \rightarrow 0, \quad h_x \rightarrow \tan \theta, \quad q \rightarrow 0, \quad \text{as } x \rightarrow s(t).$$

The first condition is obvious and the last is a no-flux condition that ensures that no mass is lost through the contact line. To the far right, the film flattens to a constant film thickness and there is no flux,

$$(4.7) \quad h \rightarrow 1, \quad q \rightarrow 0, \quad \text{as } x \rightarrow \infty.$$

Notice that the thickness of a uniform layer is fixed to one by our choice of scalings (see section 2).

We conclude this section with two useful mass conservation properties for the sharp-interface model. First, if we integrate (4.2a) twice with respect to z and use (4.2b)–(4.2e), we obtain the following expression, which relates the evolution of the interface to the divergence of the cross-sectional flux of component A :

$$(4.8) \quad h_t + q_x = 0 \quad \text{with} \quad q = \frac{1}{2} \frac{\partial}{\partial x} \int_0^d \mu_1 dz.$$

The last condition in (4.6) together with (4.7) ensures that the area of the film cross section between the contact line and an arbitrary but fixed cutoff $\hat{x} = L_{\infty}$ remains constant,

$$(4.9) \quad \frac{d}{dt} \int_{s(t)}^{L_{\infty}} h(x, t) dx = 0,$$

or, for $L_{\infty} \rightarrow \infty$,

$$(4.10) \quad \frac{d}{dt} \int_{s(t)}^{\infty} (h(x, t) - 1) dx = \frac{ds}{dt}.$$

4.2. Thin-film approximation. We can further approximate (4.2), (4.6), (4.7) in the limit of small contact angles, $\theta \ll 1$. We introduce the scalings

$$(4.11a) \quad x = \frac{1}{\theta} \tilde{x}, \quad s = \frac{1}{\theta} \tilde{s}, \quad t = \frac{2}{\sigma \theta^4} \tilde{t},$$

$$(4.11b) \quad \mu_1 = \frac{\sigma \theta^2}{2} \tilde{\mu}, \quad q = \frac{\sigma \theta^3}{2} \tilde{q}$$

and leave z and h unchanged. Inserting these we obtain

$$(4.12a) \quad \theta^2 \tilde{\mu}_{\tilde{x}\tilde{x}} + \tilde{\mu}_{zz} = 0$$

in the domains $0 < z < h(\tilde{x}, \tilde{t})$ and $\tilde{h}(\tilde{x}, \tilde{t}) < z < d$, which is supplemented with the conditions

$$(4.12b) \quad \tilde{\mu} = \frac{h_{\tilde{x}\tilde{x}}}{(1 + \theta^2 h_{\tilde{x}}^2)^{3/2}},$$

$$(4.12c) \quad \theta^2 h_{\tilde{t}} = \frac{1}{2} (\theta^2 [\tilde{\mu}_{\tilde{x}}]_+^+ h_{\tilde{x}} - [\tilde{\mu}_z]_+^+)$$

on the sharp interface $z = h(\tilde{x}, \tilde{t})$ and

$$(4.12d) \quad \partial_z \tilde{\mu} = 0$$

on the substrates at $z = 0, d$. The relation (4.8) remains unchanged in the rescaled variables. From the leading-order parts of (4.12a), (4.12b), (4.12d), we immediately find $\tilde{\mu} = h_{\tilde{x}\tilde{x}}$, and with the leading-order part of (4.8), we obtain

$$(4.13a) \quad h_{\tilde{t}} + \tilde{q}_{\tilde{x}} = 0, \quad \text{where} \quad \tilde{q} = \frac{d}{2} h_{\tilde{x}\tilde{x}\tilde{x}}.$$

The leading-order contact line and far-field conditions are, respectively,

$$(4.13b) \quad h = 0, \quad h_{\tilde{x}} = 1, \quad \tilde{q} = 0, \quad \text{at } \tilde{x} = \tilde{s},$$

$$(4.13c) \quad h \rightarrow 1, \quad \tilde{q} \rightarrow 0 \quad \text{at } \tilde{x} \rightarrow \infty.$$

From (4.10), we get

$$(4.14) \quad \frac{d\tilde{s}}{d\tilde{t}} = \frac{d}{d\tilde{t}} \int_{\tilde{s}(\tilde{t})}^{\infty} (h(\tilde{x}, \tilde{t}) - 1) d\tilde{x}.$$

This dimension-reduced model will be used to efficiently explore the topological transformation when the equilibrium contact angle, θ , is assumed to be small. Moreover, its parameter-free form enables all the dynamics that occur when $\theta \ll 1$ to be deduced from a single numerical simulation. We will also assess the accuracy of the thin-film model by comparing it with simulations of the phase-field equations (2.5).

5. Topological transitions.

5.1. Bilayer breakup. The horizontal bilayer with an A -rich phase on top of a B -rich phase that is created in the first step is only metastable. The energy of the layer can be further decreased by reducing the length of the interface between the two phases if the bilayers are replaced by an arrangement of trapezoidal stripes. If, for example, we have a 50:50 ratio of the species, which in our scalings implies a

distance between the two substrates of $d = 2$, and we have neutral substrates, $\beta = 0$, then the only contribution to the energy comes from the interface between the phases. Moreover, the stripes are rectangular in this case. If the width of each stripe is on average w , then a total interface length of $2nd$ for $2n$ stripes replaces a single interface of length $2nw$ for the bilayer state. Thus, the energy is reduced if and only if $w > d$.

A refined energy argument, in combination with mass conservation, has been given by Hennessy et al. [12] for antisymmetric substrates with general substrate-material interface energy densities (i.e., general β). This analysis reveals additional details about the transition between the two states if the A - B interface is forced to touch one of the two substrates by a finite perturbation when $\beta < 1$. As shown in Figure 3 the newly formed contact lines retract, to either side, each collecting the A -rich phase in a growing trough. These troughs eventually hit the bottom substrate and each gives rise to a new pair of contact lines. The shed A -rich material stabilizes in a stripe, while growing rims now appear in the B -rich phase until they hit the upper substrate. The energy estimates show that the energy difference for subsequent stripe formation is less than what is needed for the formation of the first, so the process is self-sustaining: Once an initial ‘‘hole’’ is formed, the entire bilayer will transform into an array of stripes through a sequence of rupturing events. The argument also yields estimates for the width of the stripes, which are $w = 13.2/\theta$ for small contact angles and not more than $w = 13.8/\theta$ for angles up to $\pi/2$, measured at the center line.

We begin with the case where the substrate-material interface energy is weak and the equilibrium contact angle is large. Thus, we set the equilibrium contact angle equal to 90° , which is equivalent to neglecting the energy of the substrate-material interfaces. It is assumed that a bilayer has formed, for example, by slowly cooling the system, and we now investigate the dynamics of the system after this bilayer has been ruptured. The corresponding initial condition for the phase-field model is constructed with the leading-order solution of the sharp-interface problem (4.3) and taking the interface profile to be of the form

$$(5.1) \quad h(x) = \begin{cases} 2 - \sqrt{1 - (x - 1 - s_0)^2}, & s_0 < x < s_0 + 1, \\ 1, & x > s_0 + 1, \end{cases}$$

which represents a ruptured 50:50 bilayer with an initial contact line at $x = s_0$. Setting $\theta = 90^\circ$ implies $\beta = 0$. We take $\varepsilon = 0.127$ and $s_0 = 2/5$. The temperature is assumed to be constant so we set $\chi \equiv 1$. The computational domain is cut off at $L_\infty = 50$.

The results of a phase-field simulation are shown in Figure 3, and it can be seen that puncturing the bilayer will induce a topological transition into a striped state. The stripes that form are perfect rectangles as a result of the equilibrium contact angle being 90° , and the width of the second through fifth columns is 8.4, 8.2, 8.2, and 8.4, respectively. The qualitative arguments in Hennessy et al. [12] yield an estimate of 8.8 for the stripe width, which is in good agreement with the simulations. Also shown in this figure is the evolution of the free energy of the system, which for the rescaled model in (2.5) is defined at the end of Appendix A. The free energy decreases monotonically, with large jumps occurring immediately after new contact lines are created. For systems held at constant temperatures, the free energy must be a monotonically decreasing function of time, and a proof of this claim is given in Appendix A.

Reverse transformations. Assume now that the mixture is separated into n pairs of adjacent A - B columns, much like the final configuration shown in Figure 3. Using

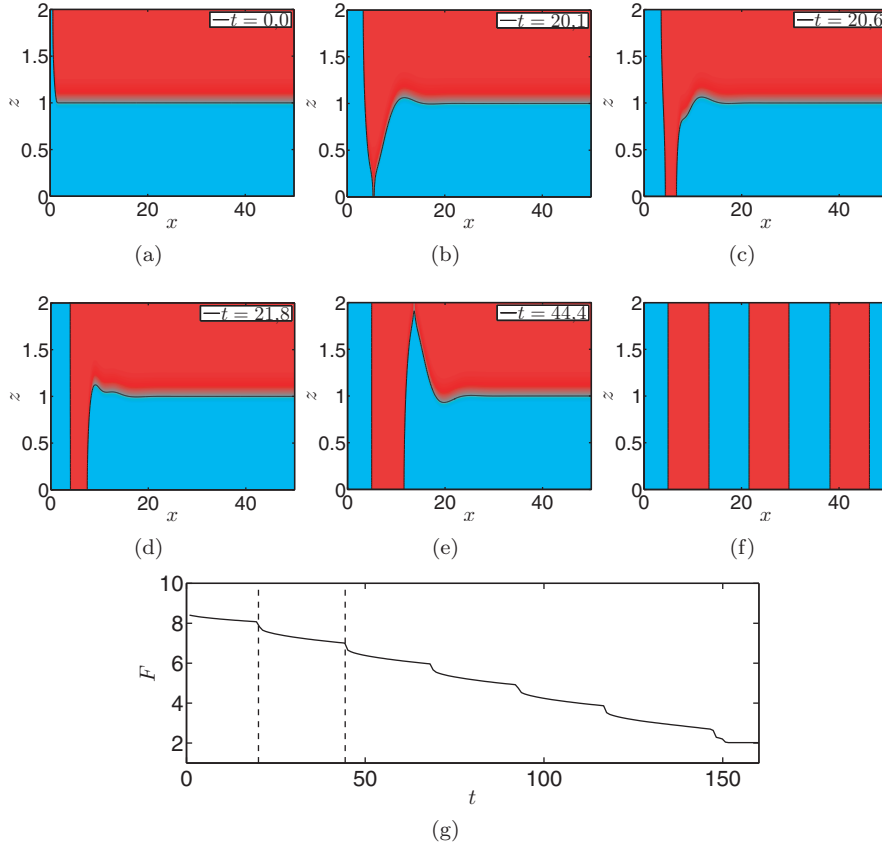


FIG. 3. (a)–(f) The subsequent evolution of the solution in Figure 1, showing, in particular, the dynamics that occur when a hole is introduced into the upper layer of A -rich material (red) so that material from the bottom layer of B -rich material (blue) comes into contact with the upper substrate (a). The hole widens and the displaced mass creates a growing dip in the top layer that eventually touches the bottom substrate (b), creating new contact lines and a hole in the bottom layer. The new hole rapidly opens ((c) and (d)), and the material that is displaced in the bottom layer forms a growing ridge that eventually comes into contact with the upper substrate (e). The process then repeats itself until the bilayer has been transformed into a sequence of columns. The solution is shown at times $t = 0$, $t = 20.2$, $t = 20.6$, $t = 21.8$, $t = 44.4$, and $t \rightarrow \infty$, i.e., the steady state. The black line corresponds to the $\phi = 0$ contour and is used to denote a sharp interface between domains. (g) The evolution of the free energy F . This can be proved to be monotonic; see Appendix A. The sharp decreases correspond to creation of new contact lines and the rapid widening of the associated holes. The dashed lines correspond to the times shown in panels (b) and (e).

the same type of qualitative argument that was presented in the previous paragraph, we find that such a configuration will not be energetically favorable compared to the bilayer if the width of each column, w , is less than the height of the channel d , i.e., if $w < d$. In such a situation, we expect that a reverse topological transition will occur if the initial state is perturbed.

To explore this scenario, we perform simulations with the phase-field model using initial conditions that correspond to a repeating sequence of A - B columns. To perturb the system and initiate the transformation, we shorten one of the columns, which has the effect of locally merging the two neighboring columns. An example of such an initial condition is shown in Figure 4(a), where two columns of material A are brought

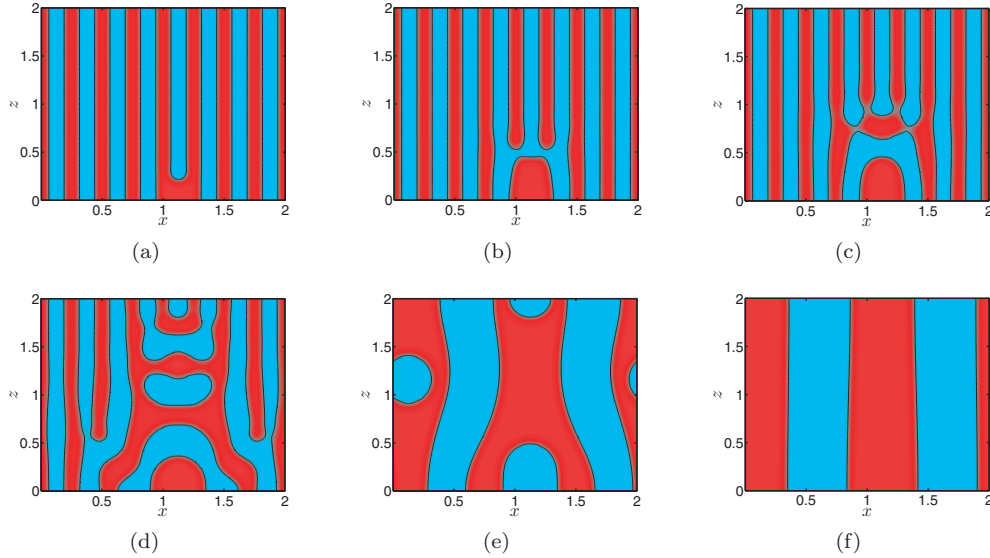


FIG. 4. *Joining two columns of A-rich material (red) initiates a rapid sequence of merging events that leads to a coarser set of columns. The columns of phase A are initially joined by creating a bridge between them at the bottom substrate, effectively shortening the column of phase B (blue) that separates them (a). The shortened column is pulled to the upper substrate to minimize its interface, but as this happens the two columns of A detach from the bridge (b). These also begin to move upward but as they do they come into contact with other columns of A (c) to initiate further detaching, merging, and coarsening events ((d) and (e)). The system then settles into a state of coarser columns (f). The solution is shown at times $t = 2.7 \times 10^{-5}$, 1.1×10^{-3} , 2.1×10^{-3} , 4.3×10^{-3} , 2.1×10^{-2} , and 0.37. The black line corresponds to the $\phi = 0$ contour. Merging two columns of the same phase in panel (f) causes the shortened column to retract; however, while it does it gets diffusively absorbed into the larger column of the same phase, resulting in a system with only one column of each phase.*

together in a system that begins as eight pairs of A - B columns. The other parameter values are $\varepsilon = 0.04$, $\chi \equiv 1$, $\beta = 0$, with $L_\infty = d = 2$. Once the perturbation is added the system evolves under the action of interface minimization and this drives the shortened B column upward and material A fills the void, thus thickening the bridge that joins the two columns of A . However, around $t = 1.1 \times 10^{-3}$ (Figure 4(b)) the two A columns pinch off from the bridge and are pulled toward the upper substrate in the same way that the shortened column of B was. Interactions between the retracting A columns and their neighbors lead to additional merging and pinch-off events (Figures 4(c) and (d)), thus creating a very complex set of dynamics. For $t = 2.1 \times 10^{-2}$ the morphology has been reduced to two pairs of deformed A - B columns, with the A columns containing pockets of material B . These pockets are diffusively absorbed into the larger B columns (Figure 4(e)), and eventually the system settles into a state consisting of two pairs of A - B columns (Figure 4(f)). This process can be repeated in principle, leading to a fast coarsening of the striped morphology.

5.1.1. Comparison to the thin-film model. For our comparisons we choose again a 50:50 ratio of the two constituents but a shallow contact angle so that the thin-film model (4.13) can be used with $d = 2$. We start from the bilayer situation where a layer of the B -rich phase has formed at the bottom surface and a layer of A -rich phase at the top, as a result, for example, of the slow quenching process discussed in section 3.

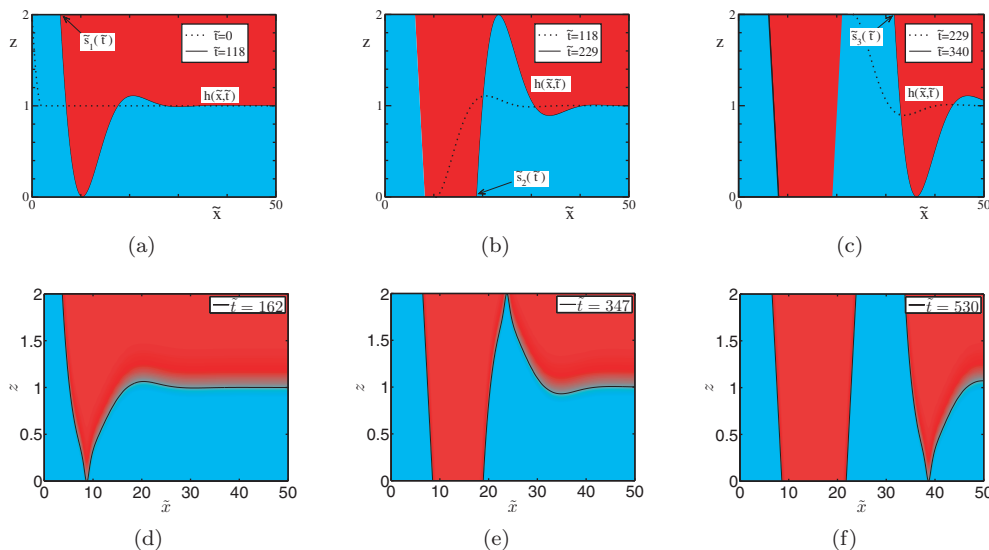


FIG. 5. Evolution of the interface between the phases after introduction of an initial hole with B -rich phase (blue) penetrating the A -rich phase (red) at $\tilde{x} = 0$, $\tilde{z} = 2$. (a)–(c) Numerical results for the thin-film model (4.13). (d)–(f) Numerical results for the phase-field model (2.5). The black lines in panels (d)–(f) denote the $\phi = 0$ contour, which corresponds to the film profile $h(\tilde{x}, \tilde{t})$ in panels (a)–(c). The initial hole widens and pushes the B -phase to the right. This entails growth of the minima and maxima in the interface, which gives rise to alternating holes in the A - and B -layers and thus the formation of new contact lines. Further details are given in the text.

For the numerical solution of the thin-film model, we truncate the domain at $\tilde{x} = L_\infty$ (with a choice for L_∞ that was larger than 100) and impose $h_{\tilde{x}} = 1$, $h_{\tilde{x}\tilde{x}} = 0$ there. At $\tilde{x} = \tilde{s}$, we impose $h = 0$ and $h_{\tilde{x}} = 1$ and require global mass conservation to hold,

$$\int_{\tilde{s}(\tilde{t})}^{L_\infty} h(\tilde{x}, \tilde{t}) d\tilde{x} = \int_{\tilde{s}(0)}^{L_\infty} h(\tilde{x}, 0) d\tilde{x}.$$

The truncated domain is mapped onto the unit interval by the linear transformation $\tilde{x} \mapsto (\tilde{x} - \tilde{s}(\tilde{t})) / (L_\infty - \tilde{s}(\tilde{t}))$ and the resulting problem is discretized using finite differences in space and implicit Euler in time. Step doubling was used to control the time discretization error. Initial conditions at $\tilde{t} = 0$ are

$$(5.2a) \quad \tilde{s} = 0, \quad h(\tilde{x}, 0) = d - h_i(\tilde{x}),$$

where

$$(5.2b) \quad h_i(\tilde{x}) = \begin{cases} \tilde{x} - \tilde{x}^2/4 & \text{for } \tilde{x} < 2, \\ 1 & \text{elsewhere.} \end{cases}$$

Notice that with this choice, we assume that initially a thin hole filled by B -rich phase has been created in the A -rich top layer, giving rise to a contact line at the top substrate, $z = d = 2$. The initial interface $z = h(\tilde{x}, 0)$ satisfies the contact angle condition $h_{\tilde{x}} = -1$ at $\tilde{x} = \tilde{s}$.

In Figure 5(a), the initial data ($\tilde{t} = 0$) is shown by a dotted line: a hole filled with B -rich material has been created in the A -rich phase. The contact line at $x = \tilde{s}_1(0) = 0$ retreats, until the minimum $\min_x h$ of the interface hits $z = 0$ at time $\tilde{t}_1 = 118$ and

position \tilde{x}_2 and forms a pair of new contact lines, one of which moves to the left, the other, labeled $\tilde{s}_2(\tilde{t})$, to the right. Thus, the B -rich layer is split into two parts. The left part settles into an equilibrium, shown in Figure 5(b), with the interface between the B - and A -rich phases located at $z = 8.14 - \tilde{x}$ as determined by conservation of the B -rich phase in the leftmost stripe.

The contact line $z = 0$, $\tilde{x} = \tilde{s}_2(\tilde{t})$ for the other part travels to the right, with a growing rim forming in the B -layer ahead of it. The interface $h(\tilde{x}, \tilde{t})$ for $\tilde{x} < \tilde{s}_2(\tilde{t})$ is obtained by restarting the simulations at $\tilde{t} = \tilde{t}_1$, with the initial position for the contact line at $\tilde{s}_2 = \tilde{x}_2$ and using $h(\tilde{x}, \tilde{t}_1)$, for $x > \tilde{s}_2(\tilde{t}_1)$ as the initial profile (indicated by a dotted line in (b)).

Eventually, in Figure 5(b), the right moving and growing ridge hits the top substrate at $\tilde{t}_3 = 229$ and $\tilde{x} = x_3$, giving rise to another pair of contact lines. This splits the A -rich layer into two parts. The left part equilibrates as a strip of A -rich phase between the old B - A interface, at $z = -\tilde{x} + 8.14$, and the new A - B interface at $z = \tilde{x} - 19.1$. The last expression follows from conservation of phase A . The contact line at $z = 2$, $\tilde{x} = \tilde{s}_3(\tilde{t})$ for right part of the A -rich layer continues to evolve, with a decreasing minimum ahead of it, that will eventually result in another rupture of the B -rich layer shown in Figure 5(c). The evolution up to this point is obtained by restarting the simulation at $\tilde{t} = \tilde{t}_3$ with $\tilde{s}_3(\tilde{t}_2) = x_2$, using $h(\tilde{x}, \tilde{t}_2)$ for $\tilde{x} > \tilde{s}_3(\tilde{t}_3)$ as the initial interface profile. As before, this initial profile is indicated in the figure by a dotted line. The width of the first equilibrated A -rich stripe is 13.0, which is very close to the prediction of 13.2 from the qualitative argument made in the beginning of this section and in [12].

The accuracy of the thin-film model can be examined by running equivalent numerical simulations using the phase-field model in (2.5) and applying the thin-film scalings in (4.11) to the results. The thin-film initial condition given in (5.2) is converted into an initial condition for the phase-field model using the leading-order composite solution for the sharp-interface model (4.3) after the appropriate rescalings have been made.

When applying the thin-film scalings a value for the equilibrium contact angle θ is needed. We choose a value of $\theta = 50^\circ$, which is large enough to allow the topological transition to be computed in a reasonable amount of time but small enough that the thin-film limit is still captured in the phase-field model. We also replace θ by $\tan \theta$ in the thin-film scalings (4.11) to account for the loss of accuracy in the small-angle approximation.

The bottom row of Figure 5 shows the results of a phase-field simulation in the thin-film limit. We have also taken $\chi \equiv 1$ and $\varepsilon = 0.2$. A contact angle of 50° corresponds to a substrate-material interface energy given by $\beta = 0.64$. The computational domain is truncated at $x = 80$, which, in the thin-film scaling, corresponds to $L_\infty = 95$.

The simulation confirms that an initial hole at the top of the bilayer can lead to a receding contact line, which, in turn, will create a growing ridge in the bottom layer. We find that at time $\tilde{t} = 162$ this ridge comes into contact with the bottom substrate and new contact lines are born at position $\tilde{x} = 8.7$ (see Figure 5(d)). The motion of the new contact line on the bottom substrate creates a ridge in the upper layer which comes into contact with the top substrate at time $\tilde{t} = 347$ (shown in Figure 5(e)). The two contact lines on the bottom substrate settle into their equilibrium positions at $\tilde{x} = 8.6$ and $\tilde{x} = 21.9$. Moreover, the new contact line on the upper substrate creates another ridge in the lower layer which comes into contact with the bottom substrate at time $\tilde{t} = 530$. This is shown in Figure 5(f).

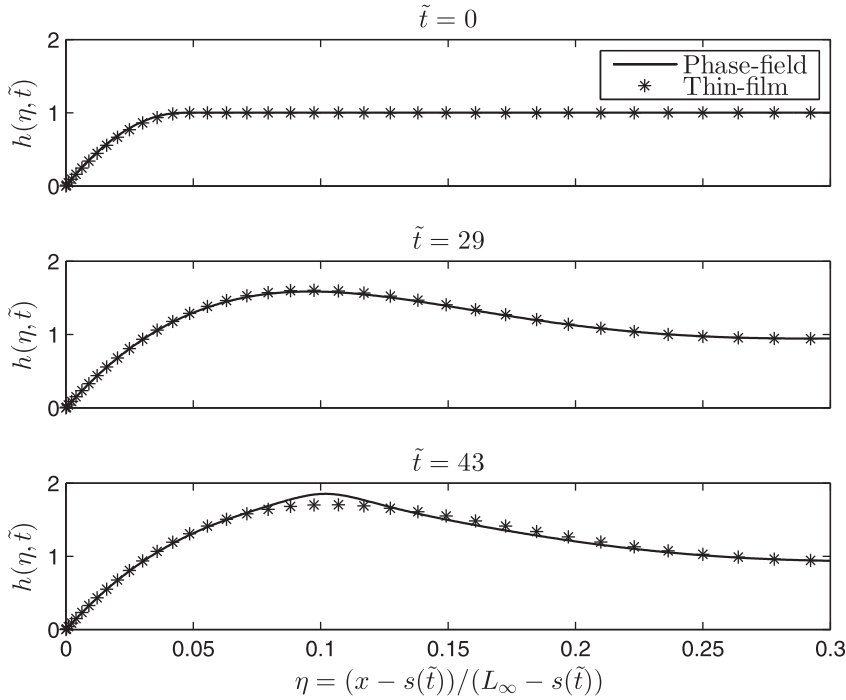


FIG. 6. Comparison of the bilayer interface profiles computed using the phase-field and thin-film models when the equilibrium contact angle is set to $\theta = 20^\circ$. Before the system is close to a topological transition ($\tilde{t} \leq 29$), the agreement between the two models is excellent. However, when the maximum of the ridge is within an $O(\varepsilon)$ distance from the upper substrate ($\tilde{t} = 43$), a “suction” effect pulls the interface upward in the phase-field model, making the transition occur sooner than in the thin-film model, where this effect is absent.

We have continued the phase-field simulation until the topological transition is complete and the bilayer has been transformed into a series of trapezoidal columns. The widths of the second through fifth columns as measured from the line $z = 1$ are given by 15.3, 15.0, 15.0, and 14.8, respectively. These values are in good agreement with the predicted value of 13.5 obtained by qualitative arguments.

From these results we conclude that the thin-film and phase-field models agree remarkably well on the geometrical aspects of the topological transition. However, when comparing when each transition occurs in the two models, we see that there are significant quantitative discrepancies. To test whether these differences are a consequence of using a large contact angle in the phase-field model which might prevent the thin-film regime from being accurately captured, the first topological transition has been computed with the equilibrium contact angle reduced to 20° . All the other parameters are kept the same as above. Figure 6 compares the interface profiles computed using the phase-field and thin-film models at various times. The agreement between the models is excellent for $\tilde{t} \leq 29$; however, differences in the solutions exist for larger times. The source of this discrepancy is due to an apparent “suction” effect that occurs in the phase-field model when the interfacial ridge gets within an $O(\varepsilon)$ distance from the upper substrate. This effectively pulls the ridge up toward the substrate, making the topological transition occur sooner in the phase-field model than in the thin-film model, where this suction effect is absent. Thus, the discrepancy between the times of the topological transitions is not necessarily due to the phase-field model

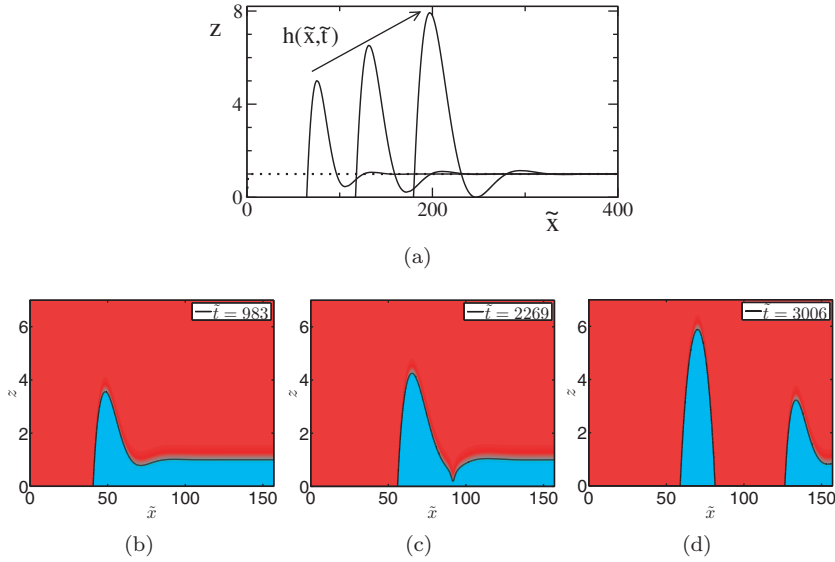


FIG. 7. Evolution of the interface between the two phases in the thin-film (top) and phase-field (bottom) models when the initial layers are not of equal thickness. When this is the case, the location of the second hole depends on the relative thickness of the layers. In both simulations shown here, the upper layer is sufficiently thick that the second hole is nucleated on the lower substrate, causing a drop to form instead of a column. (a) Simulation of the thin-film model. The initial condition is denoted by a dotted line, and three profiles are shown at times $\tilde{t} = 2 \times 10^3$, 8×10^3 , and 2.2×10^4 by solid lines. The corresponding contact line positions are $\tilde{s} = 64.4$, 117, and 180, respectively. The arrow indicates the direction of time. The last profile is taken at the moment where the minimum touches $z = 0$, and the height of the ridge at this time is 7.91. (b)–(d) Simulation of the phase-field model with an equilibrium contact angle of 45° . When the minimum ahead of the rim is within an $O(\varepsilon)$ distance from the lower substrate, the rim is rapidly pinched off from the layer, which stunts the growth of the ridge. Here, the height of the ridge is approximately 4.3 when the rim detaches, which is much smaller than the corresponding height in the thin-film model. Domains of A-rich and B-rich material are red and blue, respectively. The black line corresponds to the $\phi = 0$ contour.

being outside of the thin-film regime, but rather it is caused by substrate-interface interactions that are neglected in the sharp-interface and thin-film models.

Competition between layer thickness and rim shedding. We can use the thin-film model to explore what happens if the initial horizontal bilayer configuration does not have an A-B ratio that is 50:50, in which case one of the layers will be thicker than the other. If we consider a receding contact line at the bottom interface, then by setting d to a value larger than two, we have a situation where the top, i.e., the A-rich, layer is thicker. The receding contact line forms a rim that eventually hits the top substrate, provided $d < 7.91$. For larger d , the minimum immediately following the rim hits the bottom substrate first; see Figure 7(a). Then, material is separated from the layer similar to the shedding observed by Wong et al. [31] for surface diffusion. The material that is left behind equilibrates into a droplet configuration that typically touches only one of the two substrates, rather than both as for the stripes. The numerical results in Figure 7(a) were obtained for the thin-film model (4.13) with initial condition $\tilde{s} = 0$, $h(\tilde{x}, 0) = h_i(\tilde{x})$, with h_i as in (5.2b). The channel height was set to $d = 20$, although the same results would be obtained for any $d > 7.91$ but with different values of \tilde{t} . This behavior is to be expected for thin-film equations with mobility $n < 3/2$, as shown by King and Bowen [19] and Dziwnik et al. [9].

The same rim-shedding behavior can also be observed in the phase-field model; see Figures 7(b)–(d). In this case the thickness ratio of the upper to lower layers was chosen to be 9:1, and the initial condition was formed using (5.2b) together with (4.3). The equilibrium contact angle was set to 45° with $\varepsilon = 0.32$. The dynamics share some quantitative and qualitative similarities with the thin-film model. By monitoring the position of the contact line before the rim detaches, we find that it converges to the $t^{2/5}$ behavior that is predicted from an asymptotic analysis of the thin-film equation [9, 10]. However, a key difference between the models arises when the minimum that follows the rim gets within an $O(\varepsilon)$ distance from the lower substrate, as the rim in the phase-field model is then rapidly pinched off from the main layer (Figure 7(b)). This causes the rim to detach much sooner than it does in the thin-film model and as a consequence the growth of the ridge is stunted. In this simulation the height of the ridge when the rim detaches is approximately 4.3, which is significantly smaller than the value of 7.9 found using the thin-film model. Upon detaching from the layer, the rim evolves under the action of interface minimization to form a droplet with a height that is greater than the ridge of the rim; in this case the steady state height of the droplet is approximately 6.2. If the thickness of the upper layer is sufficiently small, the top of the droplet will come into contact with the upper substrate and a column will form. This suggests that for certain thickness ratios, the transformation from a bilayer to a sequence of columns occurs via the intermediate processes of rim shedding and droplet formation.

6. Conclusions and outlook. In this paper, we considered substrate-induced phase separation and the dynamics of the interfaces for a binary mixture in a thin film geometry, with a substrate at the top and bottom but unconfined in the lateral direction. Using a Cahn–Hilliard model that includes appropriate contributions from the substrate-material interfaces, we explored the conditions under which multilayer domains form that are separated by thin interface regions. In particular, we established when the cooling of the mixture below the critical temperature gives rise to exactly two horizontal layers.

We show that a finite-size perturbation, specifically a hole in one of the layers, initiates a cascade of transitions into a vertically striped state. While this is analyzed via direct numerical simulation of the initial boundary value problem for the Cahn–Hilliard model, we exploit the multiple length scale separation to derive successively a sharp-interface model and its corresponding thin-film approximation, and we investigated the validity as an approximation to the original phase-field model.

The thin-film model we have derived belongs to a class of parabolic PDEs for which we can draw on a rich body of literature. For example, King and Bowen [19] showed that a thin-film model with mobility of h^n with $n < 3$ is consistent with a moving contact line and a finite contact angle. Moreover, for dewetting problems, it was shown that for a quadratic mobility, the static contact angle imposed by the intermolecular potential also applies to the case where the contact line recedes [22], and that the microscopic static contact angle is preserved [10]. Similar arguments can be given for $n = 0$, as is the case here, thus lending support to the assumption made here that the static contact angle carries over to the dynamical (diffusive) case. Our analysis, which is two-dimensional, will benefit even more the study of application-relevant three-dimensional counterparts, since now we can exploit our new dimension-reduced thin-film model. A well-known example is the symmetry-breaking fingering instability of a receding front in a three-dimensional setting [19, 29, 16, 9].

The combination of the phase-field, sharp-interface, and thin-film models developed here provides efficient descriptions of structure formation as well as long-time

dynamics. For example, if one of the horizontal layers is much thinner than the other, the thin-film model reveals that the cascading rupture events will occur in the thinner of the two layers only by repeated shedding of the rim, thus leading to an array of droplets of the minority phase rather than a series of vertical stripes. While for antisymmetric substrates the stripes have straight edges, suggesting a very slow coarsening of the domains, for symmetric substrate configurations the stripes are lens-like. It would be interesting to look at the coarsening behavior and how it can be captured by the sharp-interface or thin-film model. If, on the other hand, we start from a structured state with sufficiently narrowly spaced vertical stripes, a fast coarsening occurs by merging stripes once initiated by a suitable perturbation. All this demonstrates how the interplay of geometrical confinement, bulk phase separation, and interface energy effects gives rise to a large variety of structure-forming processes that can be tuned to achieve design goals for specific technological applications.

Appendix A. Proof of monotonically decreasing free energy. The evolution of the phase-field model given by

$$(A.1a) \quad \phi_t = \nabla \cdot [(1 - \phi^2)\nabla\mu],$$

$$(A.1b) \quad \mu = \frac{1}{T} [f'(\phi) - \varepsilon^2\Delta\phi]$$

with boundary conditions

$$(A.1c) \quad \mu_z = 0, \quad \varepsilon\phi_z = f'_0(\phi) \quad \text{at } z = 0,$$

$$(A.1d) \quad \mu_z = 0, \quad \varepsilon\phi_z = f'_0(-\phi) \quad \text{at } z = d,$$

is such that it monotonically decreases the free energy of the system when the temperature is held at a fixed value. The free energy for this system is given by

$$\begin{aligned} \frac{F[\phi]}{T} &= \frac{1}{T} \int_0^d \int_{-\infty}^{+\infty} f(\phi(x, z)) + \frac{\varepsilon^2}{2} |\nabla\phi(x, z, t)|^2 \, dx dz \\ &\quad + \frac{\varepsilon}{T} \int_{-\infty}^{+\infty} f_0(\phi(x, 0, t)) \, dx + \frac{\varepsilon}{T} \int_{+\infty}^{-\infty} f_0(-\phi(x, d, t)) \, dx. \end{aligned}$$

To see that this is a monotonically decreasing function of time, we differentiate with respect to time and apply the divergence theorem to obtain

$$(A.2) \quad \begin{aligned} \frac{1}{T} \frac{dF}{dt} &= \frac{1}{T} \int_0^d \int_{-\infty}^{+\infty} [f'(\phi) - \varepsilon^2\Delta\phi] \phi_t \, dx dz \\ &\quad + \frac{\varepsilon}{T} \int_{-\infty}^{+\infty} [-\varepsilon\phi_z(x, 0) + f'_0(\phi(x, 0, t))] \phi_t(x, 0, t) \, dx \\ &\quad + \frac{\varepsilon}{T} \int_{+\infty}^{-\infty} [\varepsilon\phi_z(x, d, t) - f'_0(-\phi(x, d, t))] \phi_t(x, d, t) \, dx. \end{aligned}$$

The boundary integrals vanish due to the boundary conditions in (A.1c) and (A.1d), and using the bulk equations (A.1a) and (A.1b), this expression can be simplified to

$$(A.3) \quad \frac{1}{T} \frac{dF}{dt} = \int_0^d \int_{-\infty}^{+\infty} \mu \nabla \cdot [(1 - \phi^2)\nabla\mu] \, dx dz.$$

Another application of the divergence theorem yields

$$(A.4) \quad \frac{1}{T} \frac{dF}{dt} = - \int_0^d \int_{-\infty}^{+\infty} (1 - \phi^2) |\nabla \mu|^2 dx dz,$$

where the boundary terms vanish because of the no-flux conditions on the substrates. Assuming the order parameter satisfies $-1 \leq \phi \leq 1$, we have

$$(A.5) \quad \frac{1}{T} \frac{dF}{dt} \leq 0,$$

thus completing the proof.

The same result also holds for the rescaled system in (2.5) which has a free energy given by (after dropping the hats)

$$(A.6) \quad \begin{aligned} F = & \int_0^d \int_{-\infty}^{+\infty} f(\phi(x, z)) + \frac{\varepsilon^2}{2} |\nabla \phi(x, z, t)|^2 dx dz \\ & + \varepsilon \int_{-\infty}^{+\infty} f_0(\phi(x, 0, t)) dx + \varepsilon \int_{+\infty}^{-\infty} f_0(-\phi(x, d, t)) dx. \end{aligned}$$

Acknowledgments. The authors thank Maciek Korzec (Technische Universität Berlin) for his help with the spectral code for the CH equation. Barbara Wagner acknowledges the hospitality of OCCAM.

REFERENCES

- [1] N. D. ALIKAKOS, P. W. BATES, AND X. CHEN, *Convergence of the Cahn-Hilliard equation to the Hele-Shaw model*, Arch. Ration. Mech. Anal., 128 (1994), pp. 165–205.
- [2] K. BINDER AND P. FRATZL, *Spinodal decomposition*, in Phase Transformations in Materials, G. Kostorz, ed., Wiley, Weinheim, 2001, pp. 409–480.
- [3] K. BINDER, M. MÜLLER, AND R. L. C. VINK, *Phase behavior of polymer-containing systems: Recent advances through computer simulation*, Macromolecular Theory and Simulations, 20 (2011), pp. 600–613.
- [4] G. BROWN AND A. CHAKRABARTI, *Phase separation dynamics in off-critical polymer blends*, J. Chem. Phys., 98 (1993), pp. 2451–2458.
- [5] J. W. CAHN, *On spinodal decomposition*, Acta Metallurgica, 9 (1961), pp. 795–801.
- [6] J. W. CAHN, *Critical point wetting*, J. Chem. Phys., 66 (1977), pp. 3667–3672.
- [7] J. W. CAHN AND J. E. HILLIARD, *Free energy of a nonuniform system. I. Interfacial free energy*, J. Chem. Phys., 28 (1958), pp. 258–267.
- [8] X. F. CHEN, *Global asymptotic limit of solutions of the Cahn-Hilliard equation*, J. Differential Geom., 44 (1996), pp. 262–311.
- [9] M. DZIWNİK, M. KORZEC, A. MÜNCH, AND B. WAGNER, *Stability analysis of non-constant base state in thin-film equations*, Multiscale Model. Simul., 12 (2014), pp. 755–780.
- [10] J. C. FLITTON AND J. R. KING, *Surface-Tension-Driven Dewetting of Newtonian and Power-Law Fluids*, J. Eng. Math., 50 (2004), pp. 241–266.
- [11] M. GURTIN, *Generalized Phase Field Theories*, Department of Mathematical Sciences, Carnegie Mellon University, 1994.
- [12] M. G. HENNESSY, V. M. BURLAKOV, A. MÜNCH, B. WAGNER, AND A. GORIELY, *Propagating topological transformations in thin immiscible bilayer films*, Europhys. Lett., 105 (2014), 66001.
- [13] S. Y. HERIOT AND A. L. JONES, *An interfacial instability in a transient wetting layer leads to lateral phase separation in thin spin-cast polymer-blend films*, Nature Materials, 4 (2005), pp. 782–786.
- [14] J. JACZEWSKA, A. BUDKOWSKI, A. BERNASIK, E. MOONS, AND J. RYSZ, *Polymer vs solvent diagram of film structures formed in spin-cast poly(3-alkylthiophene) blends*, Macromolecules, 41 (2008), pp. 4802–4810.

- [15] P. K. JAISWAL, K. BINDER, AND S. PURI, *Formation of metastable structures by phase separation triggered by initial composition gradients in thin films*, J. Chem. Phys., 137 (2012), 064704.
- [16] S. JIANG, L. AN, B. JIANG, AND B. A. WOLF, *Liquid-liquid phase behavior of toluene/polyethylene oxide/poly(ethylene oxide-*b*-dimethylsiloxane) polymer-containing ternary mixtures*, Phys. Chemistry Chemical Phys., 5 (2003), pp. 2066–2071.
- [17] R. A. L. JONES, L. J. NORTON, E. J. KRAMER, F. S. BATES, AND P. WILTZIUS, *Surface-directed spinodal decomposition*, Phys. Rev. Lett., 66 (1991), pp. 1326–1329.
- [18] P. JUKES, S. HERIOT, J. SHARP, AND R. JONES, *Time-resolved light scattering studies of phase separation in thin film semiconducting polymer blends during spin-coating*, Macromolecules, 38 (2005), pp. 2030–2032.
- [19] J. R. KING AND M. BOWEN, *Moving boundary problems and non-uniqueness for the thin film equation*, European J. Appl. Math., 12 (2001), pp. 321–356.
- [20] G. KRAUSCH, *Surface induced self assembly in thin polymer films*, Materials Science and Engineering R Reports, 14 (1995), pp. 1–94.
- [21] L. MODICA, *Gradient theory of phase-transitions with boundary contact energy*, Ann. L Inst. H. Poincaré-Anal. Non Linéaire, 4 (1987), pp. 487–512.
- [22] A. MÜNCH, B. WAGNER, AND T. P. WITELSKI, *Lubrication models with small to large slip lengths*, J. Engrg. Math., 53 (2006), pp. 359–383.
- [23] B. NESTLER AND A. CHOUDHURY, *Phase-field modeling of multi-component systems*, Current Opinion in Solid State and Materials Science, 15 (2011), pp. 93–105.
- [24] A. NOVICK-COHEN, *The Cahn–Hilliard equation*, in Handbook of Differential Equations: Evolutionary Equations, vol. 4, Elsevier, New York, 2008, pp. 201–228.
- [25] R. L. PEGO, *Front migration in the nonlinear Cahn–Hilliard equation*, Proc. R. Soc. Lond. Ser. A. Math. Phys. Sci., 422 (1989), pp. 261–278.
- [26] O. PENROSE AND P. C. FIFE, *Thermodynamically consistent models of phase-field type for the kinetic of phase transitions*, Phys. D, 43 (1990), pp. 44–62.
- [27] S. PURI AND K. BINDER, *Surface effects on spinodal decomposition in binary mixtures and the interplay with wetting phenomena*, Phys. Rev. E, 49 (1994), pp. 5359–5377.
- [28] S. PURI, K. BINDER, AND H. L. FRISCH, *Surface effects on spinodal decomposition in binary mixtures: The case with long-ranged surface fields*, Phys. Rev. E, 56 (1997), pp. 6691–7000.
- [29] G. REITER AND A. SHARMA, *Auto-optimization of dewetting rates by rim instabilities in slipping polymer films*, Phys. Rev. Lett., 87 (2001), 166103.
- [30] M. SPRENGER, S. WALHEIM, AND A. B. U. STEINER, *Hierarchical structure formation in binary and ternary polymer blends*, Interface Sci., 11 (2003), pp. 225–235.
- [31] H. WONG, P. VOORHEES, M. MIKSIK, AND S. DAVIS, *Periodic mass shedding of a retracting solid film step*, Acta Materialia, 48 (2000), pp. 1719–1728.
- [32] X. XU AND X. WANG, *Analysis of wetting and contact angle hysteresis on chemically patterned surfaces*, SIAM J. Appl. Math., 71 (2011), pp. 1753–1779.
- [33] L.-T. YAN, J. LI, Y. LI, AND X.-M. XIE, *Kinetic pathway of pattern-directed phase separation in binary polymer mixture films*, Macromolecules, 41 (2008), pp. 3605–3612.